



A two-phase two-component slurry model of the F-layer at the base of Earth's core

Fryderyk Wilczyński^a, Christopher J. Davies^{a, *}, Christopher A. Jones^b

^a School of Earth and Environment, University of Leeds, Leeds LS2 9JT, UK

^b Department of Applied Mathematics, University of Leeds, Leeds LS2 9JT, UK

ARTICLE INFO

Editor: J. Badro

Keywords:

F-layer
Earth core
Slurry
Two-phase flow

ABSTRACT

We present a new two-phase two-component slurry model of the F-layer at the base of Earth's liquid outer core. Seismic observations indicate that the F-layer is stably stratified, which challenges conventional models of core dynamics that assume outer core convection and dynamo action are powered by heat and light element release at the inner core boundary (ICB). Previous work (Wong et al., 2021) has shown that an F-layer comprising a "snow" of solid iron particles falling through an iron-oxygen liquid can account for the inferred thickness, density and velocity anomaly of the F-layer; however, the model prescribed simplified fluid dynamical descriptions of the solid and liquid phases. Here we build on the work of Wong et al. (2021) by incorporating a self-consistent description of two-phase fluid dynamics. Analysing a suite of 1D time-independent solutions reveals that the solid fraction ϕ^s and liquid velocity u^l decrease with increasing bulk oxygen concentration and buoyancy number B , while ϕ^s and u^l increase with increasing ICB heat flux and solid/liquid viscosity ratio λ_η . Extrapolating to core conditions suggests that $\phi^s, u^l \ll 1$ while the solid velocity u^s is comparable to velocities at the top of the liquid core inferred from geomagnetic secular variation. Our results suggest that stable stratification in the F-layer arises from compositional variations maintained by outward barodiffusion and flux of light element that balance the inward flux of solid.

1. Introduction

The F-layer is a 150-400 km- thick region at the base of Earth's liquid outer core that is characterised by a decrease in compressional wave velocity gradient compared to the Preliminary Reference Earth Model (PREM) (Dziewonski and Anderson, 1981; Souriau and Poupinet, 1991; Ohtaki and Kaneshima, 2015; Adam et al., 2018). The anomalous velocity is usually attributed to an increase in density (e.g. Gubbins et al., 2008), and since the PREM density follows an approximately adiabatic and chemically well-mixed profile the velocity observations indicate that the F-layer is stably stratified. Elucidating the origin and dynamics of the F-layer has important implications for the geodynamo, which is thought to be powered (at present) by the release of latent heat and light elements at the inner core boundary (ICB) (e.g. Nimmo, 2015). Since both of these buoyancy sources are destabilising, the key issue is to establish how the heat and light material can pass through the F-layer without mixing away the stable stratification.

Various mechanisms have been proposed to explain the existence of the F-layer. Melting the solid core, driven either by a translational mode of inner core convection (Alboussiere et al., 2010) or by lateral variations in outer core convection originating from heterogeneous lower mantle heat flow (Gubbins et al., 2011), may produce a dense layer of iron-rich fluid surrounding the ICB though the thickness and seismic properties of such a layer are unclear. Moreover, mineralogical and dynamical studies suggest that conditions in the inner core are currently stable to thermal (Davies et al., 2015), compositional (Labrosse, 2014), and double-diffusive (Deguen et al., 2018) convection, while some simulations of rapidly rotating core convection suggest that mantle heat flow anomalies do not penetrate to the ICB (Davies and Mound, 2019). Other possibilities have invoked the presence of a solid phase. A pure iron slurry F-layer comprising a "snow" of iron particles predicts a low solid fraction (Zhang et al., 2019; Wilczyński et al., 2023) that does not match seismic observations (Gubbins et al., 2008). High solid fractions produce a mushy zone, a coherent solid matrix with residual fluid situated in pore spaces, though such a region would need to be configured

* Corresponding author.

E-mail address: c.davies@leeds.ac.uk (C.J. Davies).

<https://doi.org/10.1016/j.epsl.2024.119196>

Received 22 May 2024; Received in revised form 28 September 2024; Accepted 30 December 2024

so as to not produce top-side reflections, impedance contrasts, or shear waves that would otherwise be detected by seismology. Moreover, a thick mush is expected to collapse under its own weight (Deguen et al., 2007), resulting in an $O(1)$ km-thick layer that is too thin to match the F-layer observations.

The model presented in this paper assumes that chemical variations are critical to explaining the anomalous F-layer. Gubbins et al. (2008) argued that the F-layer is a thermo-chemical boundary layer constrained to the liquidus temperature with a light element concentration that increases with height above the ICB; however, their model did not explain the origin of the imposed compositional variation. Wong et al. (2018) and Wong et al. (2021) resolved this issue using a two-phase thermo-chemical model in which the outward transport of light element was facilitated by the falling of iron snow particles under gravity throughout the F-layer. Their model assumes phase equilibrium, i.e. that melting and freezing of solid is instantaneous, and assumes a snow of pure iron particles, which is consistent with a core composition in which oxygen (Alfè et al., 2002) or carbon (Li et al., 2019) is the primary element responsible for the observed density difference $\Delta\rho$ between solid and liquid cores. Wong et al. (2021) found stably stratified solutions that matched the observed F-layer thickness and $\Delta\rho$, and were compatible with estimates of the total CMB heat flux and inner core age (the inner core forming both from direct freezing at the ICB and falling snow). However, their model focused on the thermodynamics of the layer and assumed relatively simple fluid dynamics: a quiescent liquid phase and solid particles falling at the Stokes velocity.

The present work builds on our recent self-consistent fluid dynamical model of a two-phase pure slurry F-layer (Wilczyński et al., 2023, hereafter WDJ). The model, described in greater detail below, assumes phase equilibrium and considers the non-rotating and non-magnetic flow of compressible solid and liquid phases represented as interpenetrating continua. WDJ considered 1D time-independent solutions representing motion along the vertical direction, which enabled a broad sampling of the parameter space and detailed comparison to theoretical predictions and so we follow this approach here. Physically, we might expect that radial variations will dominate the signals obtained by seismology because the inferred density anomalies are many orders of magnitude larger than the thermo-chemical anomalies that drive core convection (Stevenson, 1987). These simple solutions serve as a natural starting point from which to build more detailed dynamical models of the F-layer.

This paper presents two extensions to the model of WDJ that make it more representative of Earth's F-layer. First, we generalise the boundary condition at the base of the model to account for a growing inner core. Second we add a light element to the pure iron system. Following Wong et al. (2021) we consider a binary alloy where the light element resides entirely in the liquid phase. As explained above, at least one element with this partitioning behaviour is required to explain the density contrast between inner and outer cores and so we regard this as an essential component of the model. This assumption neglects the small amount of light element that should enter the solid in order to explain the inner core density (Jephcoat and Olson, 1987); however, given the theoretical challenge of tracking the evolution of chemical composition in the solid we view this as a reasonable compromise. While acknowledging the recent body of work documenting the challenge of homogeneously nucleating solid near Earth's centre (e.g. Huguet et al., 2018; Wilson et al., 2023) we retain the assumption that the layer is in phase equilibrium (and hence remains on the liquidus) because lifting it would significantly increase the mathematical complexity of the problem and introduce a number of poorly determined input parameters.

The aim of this study is to present the general behaviour of the 1D steady solutions to the equations governing a two-phase two-component slurry in phase equilibrium. Given that key diagnostics of the F-layer (e.g. its solid fraction and phase velocities) are not currently observable, we take a general approach, treating the solid and liquid phases symmetrically in the governing equations (Bercovici et al., 2001) and varying

the material properties of the slurry over broad ranges. The emergence of a thin lower boundary layer means that solution behaviour must be extrapolated to the physical conditions of Earth's core. Solutions to the symmetric equations together with extrapolation allow us to suggest reasonable simplifications to the fully symmetric slurry equations.

This paper is organised as follows. Section 2 presents the governing dimensionless equations along with the necessary boundary conditions for the steady state 1D solutions. In section 3 we present and discuss solutions. Section 4 contains summary and conclusions.

2. Mathematical formulation

2.1. Governing equations

Our modelling approach is based on the continuum theory of two-phase mixtures (see e.g. Drew, 1983; Roberts and Loper, 1987; Keller and Suckale, 2019; Wilczyński et al., 2023). The derivation of the continuum equations governing two-phase flow is lengthy and the methodology has been expounded in the aforementioned works, to which the reader is referred for more information. For completeness we provide in the Supplementary Material a derivation of the two-phase two-component equations used in this study. Here we simply state the key results and approximations.

We model the F-layer as a two-phase continuum mixture composed of two phases: solid denoted by superscript s , and liquid denoted by superscript l . Each of the two phases is a continuum thermodynamic system, and the two thermodynamic continua are interpenetrating, and interact with each other via mass, momentum and energy exchanges. The relative amount of each phase at any point is measured by volume fraction ϕ^ε , where $\varepsilon \in \{s, l\}$. At each point in the continuum the phases are characterised by their system-scale velocity u^ε , pressure p , temperature T etc. We assume that the solid phase is pure while the liquid phase is composed of two chemical constituents (heavy and light - iron and oxygen) with ξ^l denoting the mass fraction of light chemical constituent in the liquid phase. We assume that the two phases are in phase equilibrium in that they share the same temperature, pressure, and Gibbs free energy and hence the system is on the liquidus.

Throughout this paper we consider one-dimensional dynamics that depend on the vertical z -coordinate only, i.e. $u^\varepsilon = (0, 0, u_z^\varepsilon(z, t))$. The gravity vector points in the negative z -direction. With the above assumptions the system of one-dimensional, time-dependent governing equations can be written

$$\frac{\partial(\phi^s \rho^s)}{\partial t} + \frac{\partial}{\partial z} (\phi^s \rho^s u_z^s) = \Gamma_\rho^s, \quad (2.1a)$$

$$\frac{\partial(\phi^l \rho^l)}{\partial t} + \frac{\partial}{\partial z} (\phi^l \rho^l u_z^l) = -\Gamma_\rho^s, \quad (2.1b)$$

$$\frac{\partial(\phi^l \rho^l \xi^l)}{\partial t} + \frac{\partial}{\partial z} (\phi^l \rho^l \xi^l u_z^l + J_\xi^l) = 0, \quad (2.1c)$$

$$\begin{aligned} \bar{c}_p \bar{\rho} \left(\frac{\partial T}{\partial t} + \bar{u}_z \frac{\partial T}{\partial z} \right) - \bar{\alpha} T \left(\frac{\partial p}{\partial t} + \bar{u}_z \frac{\partial p}{\partial z} \right) - L \Gamma_\rho^s + \frac{L}{T} \frac{\phi^s \rho^s \phi^l \rho^l}{\bar{\rho}} \Delta u_z \frac{\partial T}{\partial z} \\ = \frac{\partial}{\partial z} \left(\bar{k} \frac{\partial T}{\partial z} \right) + \Psi, \end{aligned} \quad (2.1d)$$

$$\begin{aligned} \phi^s \rho^s \left(\frac{\partial u_z^s}{\partial t} + u_z^s \frac{\partial u_z^s}{\partial z} \right) + \frac{1}{2} \Gamma_\rho^s \Delta u_z \\ = -\phi^s \frac{\partial p}{\partial z} - \phi^s \rho^s g - c_D \frac{\phi^s \rho^s \phi^l \rho^l}{\bar{\rho}} \Delta u_z + \frac{4}{3} \eta^s \frac{\partial}{\partial z} \left(\phi^s \frac{\partial u_z^s}{\partial z} \right), \end{aligned} \quad (2.1e)$$

$$\begin{aligned} \phi^l \rho^l \left(\frac{\partial u_z^l}{\partial t} + u_z^l \frac{\partial u_z^l}{\partial z} \right) + \frac{1}{2} \Gamma_\rho^s \Delta u_z \\ = -\phi^l \frac{\partial p}{\partial z} - \phi^l \rho^l g + c_D \frac{\phi^s \rho^s \phi^l \rho^l}{\bar{\rho}} \Delta u_z + \frac{4}{3} \eta^l \frac{\partial}{\partial z} \left(\phi^l \frac{\partial u_z^l}{\partial z} \right), \end{aligned} \quad (2.1f)$$

$$\left(\frac{1}{\rho^l} - \frac{1}{\rho^s} - \frac{\alpha_\xi^l \xi^l}{\rho^l} \right) dP = \frac{L}{T} dT + \frac{RT}{m_O} d\xi^l, \quad (2.1g)$$

$$d\rho^s = \rho^s(\beta^s dP - \alpha^s dT), \quad (2.1h)$$

$$d\rho^l = \rho^l(\beta^l dP - \alpha^l dT - \alpha_\xi^l d\xi^l). \quad (2.1i)$$

where

$$\begin{aligned} \phi^l &= 1 - \phi^s, & \Delta u_z &= u_z^s - u_z^l, & \bar{\rho} &= \phi^s \rho^s + \phi^l \rho^l, \\ \bar{c}_p &= (\phi^s c_p^s \rho^s + \phi^l c_p^l \rho^l) / \bar{\rho}, & \bar{\alpha} &= \phi^s \alpha^s + \phi^l \alpha^l, & \bar{k} &= \phi^s k^s + \phi^l k^l, \\ \bar{u}_z &= (\phi^s \rho^s u_z^s + \phi^l \rho^l u_z^l) / \bar{\rho}, \\ J_\xi^l &= -\frac{\kappa_O m_O \phi^l \rho^l \xi^l}{RT} \left(\frac{RT}{m_O \xi^l} \frac{\partial \xi^l}{\partial z} + \frac{\alpha_\xi^l}{\rho^l} \frac{\partial p}{\partial z} \right), \\ \Psi &= c_D \frac{\phi^s \rho^s \phi^l \rho^l}{\bar{\rho}} (\Delta u_z)^2 + \frac{4}{3} \eta^s \phi^s \left(\frac{\partial u_z^s}{\partial z} \right)^2 \\ &\quad + \frac{4}{3} \eta^l \phi^l \left(\frac{\partial u_z^l}{\partial z} \right)^2 + \frac{RT}{\kappa_O m_O \phi^l \rho^l \xi^l} |J_\xi^l|^2. \end{aligned} \quad (2.2)$$

The above system (2.1) comprises 9 equations for 9 variables: ϕ^s , u_z^s , u_z^l , p , T , Γ_ρ^s , ρ^s , ρ^l , ξ^l . Equations (2.1a) and (2.1b) describe conservation of mass of solid and liquid phases, where $\phi^l = 1 - \phi^s$ is the liquid volume fraction and Γ_ρ^s is solid phase production rate. Equation (2.1c) determines conservation of mass of the light element, where J_ξ^l is the diffusive flux of light element. For further reference, a table of physical parameters and values is provided in Appendix A, Table A.1.

Equation (2.1d) is the heat equation for the mixture in which temperature changes arise due to (from left to right) pressure heating, latent heat release (absorption) due to freezing (melting), transport of latent heat by phase separation (sometimes called the heat pipe term (Roberts and Loper, 1987)), thermal diffusion, and heating due to dissipative effects Ψ (viscous, frictional, and heat of reaction). Here, overbar indicates quantities, defined in (2.2), that pertain to the mixture as a whole: $\bar{\rho}$ is the mixture density, \bar{u}_z is the velocity of the mixture, \bar{c}_p is the heat capacity of the mixture, $\bar{\alpha}$ is the thermal expansion coefficient of the mixture, \bar{k} is the thermal conductivity of the mixture (where c_p^s , α^s , k^s are heat capacity, thermal expansion coefficient, thermal conductivity of phase ϵ). L is the latent heat of fusion which we assume to be constant.

Equations (2.1e), (2.1f) describe conservation of momentum and relate inertia (left hand side) to the sum of forces: the pressure gradient force, gravitational force; the force due to momentum exchange between the phases (friction), where Δu_z is the difference between the velocities of the two phases (2.2), $c_D = \eta^l / (k_\phi \rho^l)$ is a constant coefficient of inter-phase friction with $k_\phi = 5 \times 10^{-10} - 10^{-7} \text{ m}^2$ the permeability constant; and the viscous force, where η^ϵ is dynamical viscosity of phase ϵ .

Equation (2.1g) is the liquidus relation which follows from the assumption that the system is in phase equilibrium. α_ξ^l is the compositional expansion coefficient of the liquid, \mathcal{R} is the universal gas constant, and m_O is molar mass of oxygen.

Equations (2.1h), (2.1i) are equations of state that relate the specific density variations to variations of pressure, temperature and composition, where β^ϵ denotes the isothermal compressibility of phase ϵ .

It is worth noting here that the formulation above differs from that of Wong et al. (2018, 2021) in several respects because they are derived from fundamentally different starting points: diffusive mixture theory in the case of Wong et al. (2018, 2021) and the ‘two fluid’ theory in the present study. Roberts and Loper (1987) have shown how the two-fluid approach simplifies to the diffusive mixture treatment and indeed the governing equations (3)-(6) of Wong et al. (2021) can be recovered by omitting terms from the present theory. The differences lie in the assumptions that have been used. Wong et al. (2021) assume that the liquid velocity is negligibly small and neglect terms involving $d\phi^s/dz$, which allows to write an equation determining the evolution of the solid flux directly without knowledge of the solid fraction or solid velocity. The Stokes mobility model used by Wong et al. (2021) enables the solid fraction and solid velocity to be obtained from the calculated solid flux.

However, the mobility model makes a number of assumptions that are unverifiable due to a lack of observations. Here the phase velocities and solid fraction are calculated directly from general conservation equations.

2.2. Boundary conditions

To complete the theory it is necessary to specify conditions on the bounding surfaces. In general the relevant conditions at both the top and bottom of the slurry are not known because they are not constrained by observations. There are a limited number of conditions that can be deduced from the governing equations, which need to be supplemented with additional assumptions and approximations based on physical intuition or experimental insight where available.

We consider a slurry layer of fixed depth d bounded between $z = z_{ICB}$ and $z = z_{ICB} + d$, where z_{ICB} indicates the position of the ICB. As the inner core freezes, latent heat and light material are released at the ICB and the position of the ICB advances upwards (over geological timescales). The ICB velocity U_{ICB} is much smaller than flow speeds in the slurry or outer core and can therefore be considered constant when modelling the F-layer. Since U_{ICB} is poorly known we treat it as a prescribed constant using values from models of Earth’s core evolution (on the order of a few millimeters per year, Davies et al., 2015; Nimmo, 2015). In this case, we may perform a Galilean transformation to change to a frame of reference that moves with the ICB (Gubbins et al., 2008). Thus, the time-dependence of a moving boundary is removed and we can consider steady (time-independent) solutions.

In general, it is possible to obtain continuity conditions that must hold on a moving boundary by integrating the governing equations over a pill-box volume that straddles the boundary and moves together with it. Applying this procedure on the ICB provides conditions determining continuity of mass flux for each of the two phases, light element flux, and internal energy flux. We assume that the inner core is completely solid and motionless and that the mean ICB position is determined by direct freezing. A complete development of the boundary conditions in the moving frame using these assumptions is given in the Supplementary Material. In the reference frame moving with U_{ICB} , the conditions can be written

$$\rho^s = \rho_r^s, \quad \rho^l = \rho_r^l \quad \text{on} \quad z = 0, \quad (2.3a)$$

$$u_z^s = 0, \quad \phi^l \rho^l u_z^l = -\rho^s U_{ICB} \quad \text{on} \quad z = 0, \quad (2.3b)$$

$$\rho^l \phi^l \xi^l u_z^l + J_\xi^l = \rho^l \phi^l \xi^l U_{ICB} \quad \text{on} \quad z = 0, \quad (2.3c)$$

$$\bar{k} \frac{dT}{dz} = -q \quad \text{on} \quad z = 0. \quad (2.3d)$$

Equations (2.3b) state that the ICB is an impermeable boundary with $u_z^s = 0$ and liquid is consumed by the direct freezing of the inner core at a rate proportional to the ICB speed U_{ICB} . Equation (2.3c) states that the total flux of light element (advective and diffusive) at the ICB must balance the release of light elements due to direct freezing. Equation (2.3d) states that the heat flux into the slurry at the ICB is equal to the total heat flux q coming out of the inner core, which comprises of latent heat release associated with inner core freezing (proportional to U_{ICB}), conductive heat flux, and a contribution due to the release of light elements associated with inner core freezing.

The top boundary represents the interface between the F-layer slurry and the rest of the outer core. Since the liquid core is vigorously convecting, its composition and temperature do not change much over the timescales considered (Davies, 2015) and we may impose fixed oxygen concentration and fixed temperature at the top of the F-layer (Wong et al., 2021)

$$\xi^l = \xi_{core}^l, \quad \text{and} \quad T = T_r \quad \text{on} \quad z = d, \quad (2.4)$$

where ξ_{core}^l and T_r are, respectively, the reference light element concentration and the reference temperature of the bulk core. We further

assume that the top boundary is a stress-free surface where the normal stresses are set to zero (Wilczyński et al., 2023):

$$\frac{du_z^s}{dz} = \frac{du_z^l}{dz} = 0 \quad \text{on} \quad z = d. \quad (2.5)$$

2.3. Nondimensionalisation

We study time-independent solutions of the governing equations (2.1). To nondimensionalise the equations the units of density (liquid and solid) and temperature are fixed to their boundary values ρ_r^l , ρ_r^s and T_r , respectively. We scale length with the depth of the layer d , velocity with the gravitational free-fall velocity \sqrt{gd} , pressure with $\rho_r^l gd$, and the mass production term Γ_ρ^s with $\rho_r^l \sqrt{gd}$. Volume fractions ϕ^e and mass concentration ξ^l are dimensionless and bounded between 0 and 1, and thus do not require any scaling. Applying these scalings to the governing equations yields the following set of dimensionless equations

$$\lambda_\rho \frac{d}{dz} (\phi^s \rho^s u_z^s) = \Gamma_\rho^s, \quad (2.6a)$$

$$\frac{d}{dz} (\phi^l \rho^l u_z^l) = -\Gamma_\rho^s, \quad (2.6b)$$

$$\frac{d}{dz} (\phi^l \rho^l \xi^l u_z^l + J_\xi^l) = 0, \quad (2.6c)$$

$$\left(\bar{c}_p \bar{\rho} \frac{dT}{dz} - \alpha^* D \bar{\alpha} T \frac{dp}{dz} \right) \bar{u}_z - \frac{\Gamma_\rho^s}{St} + \frac{\lambda_\rho \phi^s \rho^s \phi^l \rho^l}{\bar{\rho}} \Delta u_z \frac{1}{T} \frac{dT}{dz} = \frac{1}{B Pr} \frac{d}{dz} \left(\bar{k} \frac{dT}{dz} \right) + \Psi, \quad (2.6d)$$

$$\lambda_\rho \phi^s \rho^s u_z^s \frac{du_z^s}{dz} + \frac{1}{2} \Gamma_\rho^s \Delta u_z = -\phi^s \frac{dp}{dz} - \lambda_\rho \phi^s \rho^s - K \frac{\phi^s \rho^s \phi^l \rho^l}{\bar{\rho}} \Delta u_z + \frac{4}{3} \frac{\lambda_\eta}{B} \frac{d}{dz} \left(\phi^s \frac{du_z^s}{dz} \right), \quad (2.6e)$$

$$\phi^l \rho^l u_z^l \frac{du_z^l}{dz} + \frac{1}{2} \Gamma_\rho^s \Delta u_z = -\phi^l \frac{dp}{dz} - \phi^l \rho^l + K \frac{\phi^s \rho^s \phi^l \rho^l}{\bar{\rho}} \Delta u_z + \frac{4}{3} \frac{1}{B} \frac{d}{dz} \left(\phi^l \frac{du_z^l}{dz} \right), \quad (2.6f)$$

$$\left(\frac{1}{\lambda_\rho \rho^s} - \frac{1}{\rho^l} + \frac{\alpha_\xi^l \xi^l}{\rho^l} \right) \frac{dp}{dz} + \frac{1}{St D T} \frac{dT}{dz} + \frac{1}{D \chi} T \frac{d\xi^l}{dz} = 0, \quad (2.6g)$$

$$\frac{d\rho^s}{dz} = \rho^s \left(\lambda_\beta \beta^* \frac{dp}{dz} - \lambda_\alpha \alpha^* \frac{dT}{dz} \right), \quad (2.6h)$$

$$\frac{d\rho^l}{dz} = \rho^l \left(\beta^* \frac{dp}{dz} - \alpha^* \frac{dT}{dz} - \alpha_\xi^l \frac{d\xi^l}{dz} \right). \quad (2.6i)$$

where

$$\begin{aligned} \phi^l &= 1 - \phi^s, & \Delta u_z &= u_z^s - u_z^l, & \bar{\rho} &= \lambda_\rho \phi^s \rho^s + \phi^l \rho^l, \\ \bar{c}_p &= (\lambda_{c_p} \lambda_\rho \phi^s \rho^s + \phi^l \rho^l) / \bar{\rho}, & \bar{\alpha} &= \lambda_\alpha \phi^s + \phi^l, & \bar{k} &= \lambda_k \phi^s + \phi^l, \\ \bar{u}_z &= (\lambda_\rho \phi^s \rho^s u_z^s + \phi^l \rho^l u_z^l) / \bar{\rho}, \\ J_\xi^l &= -\frac{\tau \chi}{B Pr} \frac{\phi^l \rho^l \xi^l}{T} \left(\frac{1}{\chi} \frac{T}{\xi^l} \frac{d\xi^l}{dz} + \alpha_\xi^l D \frac{1}{\rho^l} \frac{dp}{dz} \right), \end{aligned} \quad (2.7)$$

$$\begin{aligned} \Psi &= D K \frac{\phi^s \rho^s \phi^l \rho^l}{\bar{\rho}} (\Delta u_z)^2 + \frac{4D}{3B} \left\{ \lambda_\eta \phi^s \left(\frac{du_z^s}{dz} \right)^2 + \phi^l \left(\frac{du_z^l}{dz} \right)^2 \right\} \\ &+ \frac{B Pr}{\tau \chi} \frac{T}{\phi^l \rho^l \xi^l} |J_\xi^l|^2. \end{aligned}$$

Boundary conditions (2.3)–(2.5), in dimensionless form, read:

$$\rho^s = 1, \quad \rho^l = 1 \quad \text{on} \quad z = 0, \quad (2.8a)$$

$$u_z^s = 0, \quad \phi^l u_z^l = -\lambda_\rho \mathcal{U} \quad \text{on} \quad z = 0, \quad (2.8b)$$

$$\phi^l \rho^l \xi^l u_z^l + J_\xi^l = \phi^l \rho^l \xi^l \mathcal{U} \quad \text{on} \quad z = 0, \quad (2.8c)$$

$$\frac{dT}{dz} = -\theta \quad \text{on} \quad z = 0, \quad (2.8d)$$

$$T = 1, \quad \xi^l = \xi_{core}^l, \quad \frac{du_z^s}{dz} = \frac{du_z^l}{dz} = 0 \quad \text{on} \quad z = 1. \quad (2.9)$$

The dimensionless numbers are

$$\begin{aligned} B &= \sqrt{\frac{\rho_r^{l2} g d^3}{\eta^l}}, & Pr &= \frac{c_p^l \eta^l}{k^l}, & D &= \frac{g d}{c_p^l T_r}, \\ St &= \frac{c_p^l T_r}{L}, & K &= \frac{c_D \rho_r^s}{\rho_r^l \sqrt{g/d}}, \\ \mathcal{U} &= \frac{U_{ICB}}{\sqrt{gd}}, & \tau &= \frac{\rho_r^l c_p^l K O}{k^l}, & \chi &= \frac{c_p^l m O}{R}, & \theta &= \frac{q d}{k^l T_r}, \\ \alpha^* &= \alpha^l T_r, & \beta^* &= \beta^l \rho_r^l g d, \\ \lambda_\alpha &= \frac{\alpha^s}{\alpha^l}, & \lambda_\beta &= \frac{\beta^s}{\beta^l}, & \lambda_{c_p} &= \frac{c_p^s}{c_p^l}, & \lambda_\rho &= \frac{\rho_r^s}{\rho_r^l}, \\ \lambda_k &= \frac{k^s}{k^l}, & \lambda_\eta &= \frac{\eta^s}{\eta^l}. \end{aligned} \quad (2.10)$$

Parameter B quantifies the strength of the gravitational force as measured against viscous forces (based on the properties of the liquid phase); the Prandtl number Pr is the ratio of viscosity to thermal diffusivity; the dissipation number D measures the influence of compressibility/stratification; the Stefan number St measures the ratio between sensible and latent heat; K describes the effects of interphase drag/friction; θ is the dimensionless heat flux at the bottom boundary; α^* and β^* are nondimensionalised coefficients of thermal expansion and isothermal compression respectively; parameters $\{\lambda_\alpha, \lambda_\beta, \lambda_{c_p}, \lambda_\rho, \lambda_k, \lambda_\eta\}$ measure ratios of physical properties between solid and liquid phases.

Table 1 provides estimates of dimensionless parameters relevant for Earth's core (based on estimates of the dimensional parameters included in Table A.1). A detailed discussion of geophysically relevant ranges for many of the parameters is given in Wong et al. (2021) (see also Wilczyński et al., 2023). In total, there are 17 dimensionless parameters (2.10) plus α_ξ^l and ξ_{core}^l and so it is necessary to fix some of the values in order to focus on the effect of quantities that are most uncertain and/or computationally inaccessible. Thankfully many of the quantities are reasonably well known (at least to within an order of magnitude) and are computationally accessible — these are stated in the upper portion of Table 1.

The parameters we vary are in the lower portion of Table 1. The ICB heat flux θ is dominated by the latent heat from direct freezing which is estimated to be 4–6 TW according to thermal evolution models (Gubbins et al., 2004; Davies, 2015), though lower estimates of 0.8–6 TW latent heat have also been proposed (Wu et al., 2024), which gives a range of $\theta \sim 0.01 - 0.1$. These values are computationally achievable and we vary θ within these limits. The value of ξ_{core}^l is uncertain because the nature and abundance of the light elements in the core are still uncertain. Here we consider ξ_{core}^l to represent the mass fraction of oxygen since O partitions entirely into liquid iron on freezing (Alfè et al., 2002). Davies et al. (2015) find a bulk core O concentration of 2.6–5.6 wt% depending on the value of the ICB density jump. Here we systematically vary ξ_{core}^l from zero to the upper end of these estimates. The values of K , B and λ_η were discussed in Wilczyński et al. (2023). K can be varied within the estimated bounds while B and λ_η are numerically unreachable. We therefore study the nature of solutions as those parameter values are increased towards their geophysical values in hope of unveiling systematic behaviour.

The dimensionless ICB velocity \mathcal{U} is minute. Nevertheless, it has implications for the heat flux boundary condition because, even though the ICB speed is small, the amount of latent heat released is large compared with heat flux due to conduction (it is thought that latent heat

Table 1

Estimates of dimensionless numbers at core conditions (based on Table A.1), and values used in this study.

Dimensionless parameters			
Symbol	Definition	Estimate	This study
α^*	Thermal expansion coefficient	0.05	0.05
α_z^l	Compositional expansion coefficient	1.1	1.1
β^*	Isothermal compression coefficient	0.003	0.005
D	Compressibility parameter	0.2	0.1
Pr	Prandtl number	0.1	0.1
St	Stefan number	4	4
τ	Oxygen-heat diffusivity ratio	$(0.8 - 1.8) \times 10^{-3}$	10^{-3}
λ_ρ	Density ratio	1.02	1.1
λ_α	Thermal expansion ratio	0.49 — 0.94	1
λ_β	Isothermal compression ratio	1.05	1
λ_c	Specific heat capacity ratio	1.05	1
λ_k	Thermal conductivity ratio	2.67 — 6.6	1
χ	$(c_p^l m_O / \mathcal{R})$	1.38	1.38
θ	Temperature gradient at $z = 0$	0.01 — 0.1	0.04 — 0.05
ξ_{core}	Oxygen concentration in Earth's core	0.01 — 0.05	0 — 0.05
B	Buoyancy number	10^{14}	$10 - 10^4$
K	Interphase friction parameter	$10^3 - 3 \times 10^5$	$10^2 - 10^4$
λ_η	Dynamic viscosity ratio	$10^{13} - 10^{24}$	$10^2 - 10^{10}$
\mathcal{U}	Dimensionless speed of ICB	10^{-14}	$0 - 10^{-6}$

is the dominant contribution to the heat flux at the ICB (Wong et al., 2021)). On the other hand, \mathcal{U} is much smaller than the expected typical phase velocities u_z^ϵ , which are on the order $(\lambda_\rho - 1)/K$ (Wilczyński et al., 2023). Thus, $\mathcal{U} \ll 1$ is not expected to have significant effect on the bulk properties of the solutions. Furthermore, since $\mathcal{U} \ll 1$, the associated sink of liquid mass in (2.8b) and source of light element in (2.8c) are correspondingly small. We thus posit that $\mathcal{U} \ll 1$ constitutes only a slight perturbation on the $\mathcal{U} = 0$ solutions. From now on we fix $\mathcal{U} = 0$ which simplifies boundary conditions on liquid phase (2.8b) and light element flux (2.8c) to

$$u_z^s = u_z^l = 0 \quad \text{on} \quad z = 0, \quad (2.11)$$

$$\phi^l \rho^l \xi^l u_z^l + J_\xi^l = 0 \quad \text{on} \quad z = 0. \quad (2.12)$$

Note these conditions imply ϕ^l is free to vary on $z = 0$. We will return to evaluate the effects and limitations of this assumption in section 3.4 by solving the full $\mathcal{U} \neq 0$ problem.

2.4. Physical interpretation of the 1D equations

In a case of a single-phase fluid, the reference state is usually trivial: the fluid layer is motionless, with pressure given by the hydrostatic balance and temperature (and heat flux) determined by thermal conduction. In the case of a two-phase liquid-solid slurry, the situation is more complex as the two-phases move relative to one another and other forces (particularly due to solid viscosity) perturb the hydrostatic balance. Furthermore, the liquidus relation requires that the temperature follows the melting point of the alloy rather than a conduction solution. The heat equation then no longer serves to define the temperature, but instead defines the rate of phase change Γ_ρ^s . The latent heat of phase change provides a new mode of heat transport, while the rate of phase change influences the phase mass flux through mass conservation. Therefore, in a two-phase two-component slurry, even the time-independent 1D state is a complicated nonlinear problem. The characteristics of a pure slurry have been described in Wilczyński et al. (2023) where mathematical details can be found. Here we declare some of the key ideas and consider what new constraints arise from the presence of a light impurity in the liquid phase.

In general the governing equations do not admit a static solution unless the two phases have equal density; the steady state flow velocities have to be non-zero ($u_z^s \neq 0$, $u_z^l \neq 0$). On the other hand, the total mass conservation law obtained by summing equations (2.6a) and (2.6b) can

be readily integrated subject to the impenetrable boundary condition (2.11) to give

$$\overline{\rho u_z} \equiv \lambda_\rho \phi^s \rho^s u_z^s + \phi^l \rho^l u_z^l = 0, \quad (2.13)$$

and hence the mean vertical velocity of the mixture $\bar{u}_z = 0$. Since ϕ^ϵ and ρ^ϵ are positive definite, this implies that the velocities of solid and liquid phases are of opposite sign. Physically, we expect solutions where dense (solid) phase falls ($u_z^s < 0$) and the light (liquid) phase rises ($u_z^l > 0$).

To maintain a steady state distribution of solid volume fraction throughout the 1D layer the downward flux of solid must be balanced by melting. The integral of the solid mass conservation equation (2.6a) states that the total melting (freezing) within the layer must balance with the solid mass flux $\lambda_\rho \phi^s \rho^s u_z^s$ entering (leaving) the layer at the top boundary, $z = 1$. (Note that the solid flux on $z = 1$ is not imposed, but is determined as part of the solution). For downward solid flux ($u_z^s < 0$), the integral of Γ_ρ^s is negative; latent heat is consumed for melting and reduces the amount of heat conducted out of the layer at $z = 1$. Naturally, total mass conservation means that a downward solid flux must be balanced by an upward liquid mass flux for all z .

Equation (2.6c) dictates that the advective flux of light element is balanced by the diffusive flux. The diffusive flux is comprised of barodiffusion, the tendency of light elements to migrate down a pressure gradient, and chemical diffusion down the concentration gradient. Results from previous thermo-chemical models of the F-layer, which are confirmed by detailed calculations in section 3 below, suggest that stabilising density distributions require a stabilising distribution of light element i.e., increasing with height $d\xi^l/dz > 0$ (Gubbins et al., 2008; Wong et al., 2021), and so chemical diffusion is expected to transport light elements downwards. On the other hand, the pressure increases downwards ($dp/dz < 0$) and thus barodiffusion will act to transport the light elements upwards (Gubbins and Davies, 2013).

Equation (2.6c) readily integrates, subject to boundary condition (2.12) to give

$$\rho^l \phi^l \left(\xi^l u_z^l - \frac{\tau}{B Pr} \left(\frac{d\xi^l}{dz} + \alpha_\xi^l \chi D \frac{1}{\rho^l T} \frac{dp}{dz} \right) \right) = 0. \quad (2.14)$$

Equation (2.14) is a first order ODE with a much simpler form than (2.6c), and is the equation we use in numerical calculations. Equation (2.14) necessitates that, if the advective flux is upward ($\xi^l u_z^l > 0$) and the pressure is increasing with depth ($dp/dz < 0$), the gradient of light element concentration must be positive $d\xi^l/dz > 0$ — light element concentration must be increasing with height.

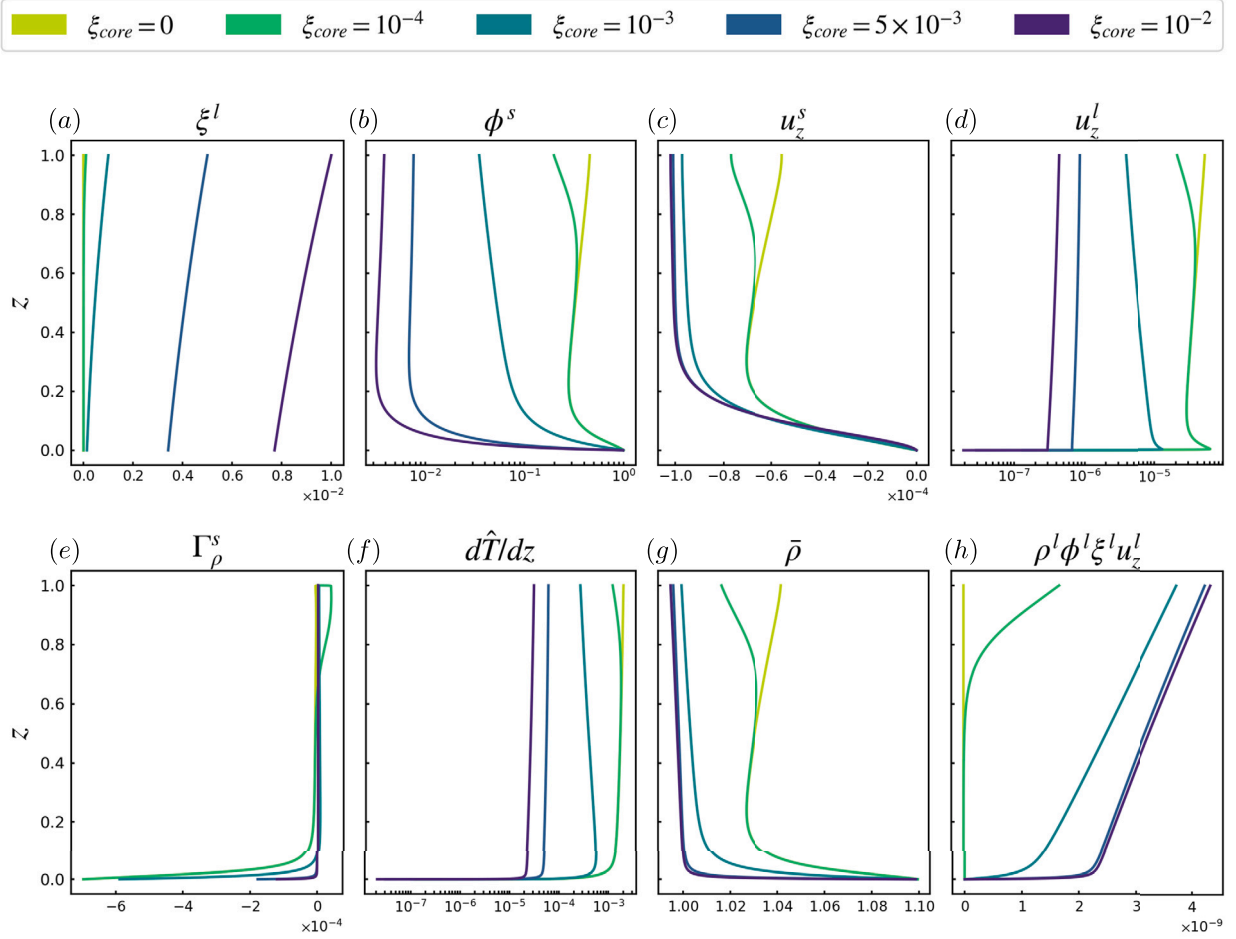


Fig. 1. Profiles of (a) concentration ξ^l ; (b) solid volume fraction ϕ^s ; (c) solid phase velocity u_z^s ; (d) liquid phase velocity u_z^l ; (e) solid mass production Γ_ρ^s ; (f) temperature gradient in excess of the conductive gradient: $d\hat{T}/dz = dT/dz + \theta$; (g) total density $\bar{\rho}$; (h) light element flux J_z^l for increasing values of the core oxygen concentration ξ_{core} ; other parameters are fixed at $B = 3 \times 10^3$, $K = 10^3$, $\lambda_\eta = 10^4$. Note that ϕ^s , u_z^s and $d\hat{T}/dz$ are plotted on logarithmic axis.

In our previous paper (Wilczyński et al., 2023) we were able to characterise the nature of pure slurry solutions and establish scaling laws for the variation of solid fraction, solid phase velocity and liquid phase velocity over the range of parameters relevant to the slurry F-layer. Considering, separately, the variation in the nature of the solutions as $B \rightarrow \infty$, or $\lambda_\eta \rightarrow \infty$, revealed two distinct regimes of limiting behaviour. In the limit of $B \rightarrow \infty$ the solutions are characterised by small values of solid fraction and liquid phase velocity $\phi^s \sim u_z^l \sim B^{-1}$, while the solid phase velocity tends to the Darcy-Stokes velocity $u_z^s \sim -(\lambda_\rho - 1)/K$ (or $u_z^s \sim k_\phi(\rho^s - \rho^l)g/(\lambda_\rho\eta^l)$ in dimensional units). On the other hand, in the limit of $\lambda_\eta \rightarrow \infty$, the solutions are characterised by small values of liquid fraction and solid phase velocity $\phi^l \sim u_z^s \sim \lambda_\eta^{-1}$, while the liquid phase velocity tends to the Darcy-Stokes velocity $u_z^l \sim (\lambda_\rho - 1)/K$. We expect that these scalings will not be altered in the presence of composition since the momentum equations from which they were derived are not changed in the presence of composition and this is verified below.

3. Solutions and analysis

3.1. Effect of light element concentration ξ_{core}

Fig. 1 shows solution profiles at increasing values of the core light element concentration ξ_{core} at fixed $K = 1000$, $B = 3000$, $\lambda_\eta = 10^4$. The general picture based on the physical interpretation of the 1D steady equations in section 2.4 is as follows. Solid material falls through the layer, $u_z^s < 0$ (Fig. 1c), and converges near the bottom boundary ($\phi^s \rightarrow 1$

as $z \rightarrow 0$, Fig. 1b). The downward flux of solid mass is balanced by an upward flow of liquid, $u_z^l > 0$ (Fig. 1d), which in turn allows for an upward advective flux of light element, $\phi^l \rho^l \xi^l u_z^l$ (Fig. 1h). Downward flow of solid and its convergence near the ICB necessitates melting in the layer, $\Gamma_\rho^s < 0$ (Fig. 1e), which consumes latent heat and reduces the heat flux conducted through the layer.

As ξ_{core} is increased, light element concentration increases throughout the layer and we observe a dramatic decrease in both the liquid velocity u_z^l and solid volume fraction ϕ^s throughout the layer. On the other hand, the solid velocity u_z^s increases in magnitude. This behaviour can be explained as follows. Increasing ξ_{core} decreases the density of the liquid phase and increases the density contrast between the solid and liquid phases. Thus, the downward negative buoyancy of the solid phase is enhanced and u_z^s increases in magnitude. Since ξ^l increases with height, the liquid phase density ρ^l is more bottom-heavy (stably stratified) than in the absence of the light element (see Fig. 1g). With enhanced density stratification, u_z^l is reduced as there is a greater energetic penalty to lift dense liquid parcels upward into less dense surroundings. From mass conservation, a natural consequence of a concurrent decrease in u_z^l and increase in $-u_z^s$ is a reduction of ϕ^s .

As ξ_{core} is increased there is less downward flux of solid and consequently less melting, which in turn reduces the amount of latent heat consumed. We define a temperature perturbation \hat{T} away from the conduction profile as follows

$$\hat{T} = T - T_{conduction}, \quad \text{where} \quad T_{conduction} = 1 + \theta(1 - z). \quad (3.1)$$

A positive gradient of the perturbation $d\hat{T}/dz$ indicates a reduction in the upward heat flux on account of latent heat consumption. At large ξ_{core} , $T \approx T_{conduction}$ and the temperature gradient thus tends to that imposed on the bottom boundary, $dT/dz \rightarrow -\theta$ (see Fig. 1f).

Mass conservation requires that the upward flux of liquid phase $\rho^l \phi^l u_z^l$ decreases in concert with the downwards flux of solid. Despite that, we observe that the light element flux $\rho^l \phi^l \xi^l u_z^l$ increases and appears to approach a limiting state as ξ_{core} is increased (see Fig. 1h). To understand this behaviour we must consider the nature of the diffusive flux J_ξ^l , which is equal and opposite to the advective flux according to eqn. (2.14). Using the liquidus relation (2.6g), the expression for J_ξ^l (2.8) can be rewritten in terms of pressure and temperature only (eliminating the dependence on ξ^l):

$$J_\xi^l = \frac{\tau\chi}{BPr} \frac{\phi^l \rho^l}{T} \left(\frac{1}{St} \frac{dT}{dz} + \left(\frac{1}{\lambda_\rho \rho^s} - \frac{1}{\rho^l} \right) D \frac{dp}{dz} \right). \quad (3.2)$$

Since increasing ξ_{core} leads to a decrease in liquid phase velocity, inertial and viscous terms in the liquid momentum equation (2.6f) become negligible. Furthermore, since ϕ^s also decreases with ξ_{core} , the friction term similarly diminishes and becomes negligible. Thus, the main balance in the liquid momentum equation is between the pressure gradient and the buoyancy, i.e. (for “large” ξ_{core})

$$\phi^l \frac{dp}{dz} \approx -\phi^l \rho^l. \quad (3.3)$$

Since both the temperature gradient and the pressure gradient tend to limiting states, so must the diffusive flux J_ξ^l (3.2).

Fig. 2(a,b,c) show the variation of solid fraction, liquid phase velocity at the top of the slurry layer (top values are representative of the bulk), and average solid phase velocity as a function of ξ_{core} for different values of θ , K and B (note that we define an average of any quantity f as $\langle f \rangle = \int_0^1 f dz$). The liquid phase velocity and solid fraction decrease with ξ_{core} and exhibit $\phi^s \sim u_z^s \sim \xi_{core}^{-1}$ scaling for sufficiently large ξ_{core} . Solid phase velocity on average increases with ξ_{core} and appears to tend to a limiting value.

The scaling of u_z^l with ξ_{core} follows from the constraint placed on the liquid velocity by the conservation of light element concentration equation (2.14), which requires balance between advective and diffusive fluxes of light element, $\phi^l \rho^l \xi^l u_z^l = -J_\xi^l$. As described above, when ξ_{core} is increased the temperature and pressure gradients and the liquid fraction tend to limiting states, and therefore so does J_ξ^l in eqn. (3.2). Thus, in the limit of “large” ξ_{core} , the average diffusive flux J_ξ^l tends to a limiting value that is independent of ξ_{core} (note that, in this case, the regime of “large” ξ_{core} is accessed at values of ξ_{core} that are smaller than the expected core light element concentration). Since $\langle J_\xi^l \rangle$ tends to a constant value as ξ_{core} is increased, it follows that $\phi^l \rho^l \xi^l u_z^l$ must also tend to an equal and opposite limiting value. It therefore follows that the velocity of the liquid phase should scale as $u_z^l \sim \xi_{core}^{-1}$.

Fig. 2(e) shows the density contrast between top and bottom of the slurry $R_\rho = \bar{\rho}(z=1)/\bar{\rho}(z=0)$; increasing ξ_{core} leads to a greater density contrast across the layer. The slurry model can produce a density contrast that is consistent with estimates of the density contrast in the F-layer, $R_\rho = 0.94 - 0.95$ (Wong et al., 2021).

Fig. 2(f) shows the maximal value of the total density gradient as a function of ξ_{core} . For ξ_{core} close to zero and sufficiently large K and B^{-1} there exist unstable solutions for which the density increases with height. Unstable solutions were also found in the pure slurry results of Wilczyński et al. (2023) for certain values of B , K and λ_η . However, as described above, increasing ξ_{core} makes the distribution of solid fraction and the liquid density more bottom heavy with lower ϕ^s at the top compared to the bottom. Similarly, at a fixed ξ_{core} the total gradient can be stabilised by increasing B . Thus, for realistic values of ξ_{core} and B we expect the solutions relevant for the F-layer to have a stable density stratification.

3.2. Role of the ICB heat flux θ

Fig. 3 shows solution profiles at increasing values of θ and fixed $K = 100$, $B = 3000$, $\lambda_\eta = 10^4$. Broadly speaking, increasing θ increases u^l and ϕ^s and reduces $|u^s|$. Increasing θ increases the pressure gradient force (through the liquidus) which acts in the direction opposite to gravity, making heavy phase fall slower, and light phase rise faster. Additionally, this increase in the pressure gradient force enhances the effects of barodiffusion and thus results in increases diffusive flux of ξ^l (see Fig. 2d). As θ is increased, the velocity of the liquid phase increases substantially (particularly close to the bottom boundary), increasing liquid advection and effectively expelling light element from the bottom portion of the domain. Between the increase of u^l and decrease of $|u^s|$, mass conservation requires that the solid volume fraction increases. Notably, increasing θ does not unsettle the stable stratification within the layer. Light element concentration increases with height and solid fraction is decreasing with height (see Figs. 1a,b) and thus the stratification must be stable.

3.3. Towards a planetary slurry: $B \gg 1$, $\lambda_\eta \gg 1$

The physical conditions of Earth’s core are characterised by values of $B = 10^{14}$ and $\lambda_\eta = 10^{13} - 10^{24}$ that are numerically unreachable. As explained in section 2.4 the slurry system exhibits distinct behaviour in the separate limits $B \rightarrow \infty$ and $\lambda_\eta \rightarrow \infty$, so it is important to establish which (if either) of these limits emerges as geophysically relevant conditions are approached. To this end we note that in the governing equations, λ_η always appears in conjunction with B , i.e. as λ_η/B . This quantity is related to the inverse of the buoyancy number based on the properties of the solid phase, $B^s = \rho_r^s (gd^3)^{1/2} / \eta^s$, through $\lambda_\eta/B = \lambda_\rho/B^s$. The ratio λ_η/B takes values in the range between $0.1 - 10^{10}$ and is therefore partially reachable numerically, so it is useful to consider the variation in solutions for increasingly large values of B at fixed values of λ_η/B (as opposed to considering variation of B at fixed λ_η).

Fig. 4 shows the variation of the solution properties as a function of B for different values of ξ_{core} , and λ_η/B , at fixed $\theta = 0.04$ and $K = 10^3$. With the exception of B , which is numerically unreachable, the parameter sweep presented in Fig. 4 uses geophysically plausible values of dimensionless parameters ξ_{core} , θ , λ_η/B and K . In Wilczyński et al. (2023) we have deduced that in the limit of large B , at fixed λ_η , the solid fraction scales like $\phi^s \sim B^{-1}$ (note that the scalings obtained in Wilczyński et al. (2023) were given in terms of a parameter R , as $\phi^s \sim R^{-1/2}$, which is related to B via $B = \sqrt{R/Pr}$). However, there is no reason to expect the same scaling to be obeyed as B and λ_η are increased concurrently (to maintain fixed λ_η/B). Remarkably, Fig. 4a shows that for some values of λ_η/B this trend is observed — when B is increased the bulk solid fraction decreases as $\phi^s \sim B^{-1}$. Similarly, the average liquid phase velocity decreases at the rate inversely proportional to B , i.e. $u_z^l \sim B^{-1}$ (Fig. 4b). Consequently, both the downward solid flux and the upward light element flux decrease as B is increased towards geophysical values (see Figs. 4d,e).

Vertical profiles at fixed $\lambda_\eta/B = 10^3$ show that solutions with increasing B tend to a state where the bulk of the layer has sparse solid fraction and small liquid velocity, while there is a thin boundary layer near the ICB where the solid fraction is substantial (Fig. 5). The reduction in ϕ^s together with the decrease in du_z^s/dz as B increases shows that the total stress $\sigma = \phi^l \sigma^l + \phi^s \sigma^s$ becomes dominated by the liquid contribution, as expected given the diminishing solid fraction. Since the solid fraction decreases with increasing B , so does the solid mass flux even though solid phase velocities tend to limiting values (see Fig. 4a,c,d). The light element flux is also small (Fig. 4e), though in this case the liquid fraction tends towards unity with increasing B while the liquid phase velocity decreases. Nonetheless, this movement of phases is critical in maintaining stable density stratification while allowing for light element advection upwards. Thus, on the whole, the F-layer can

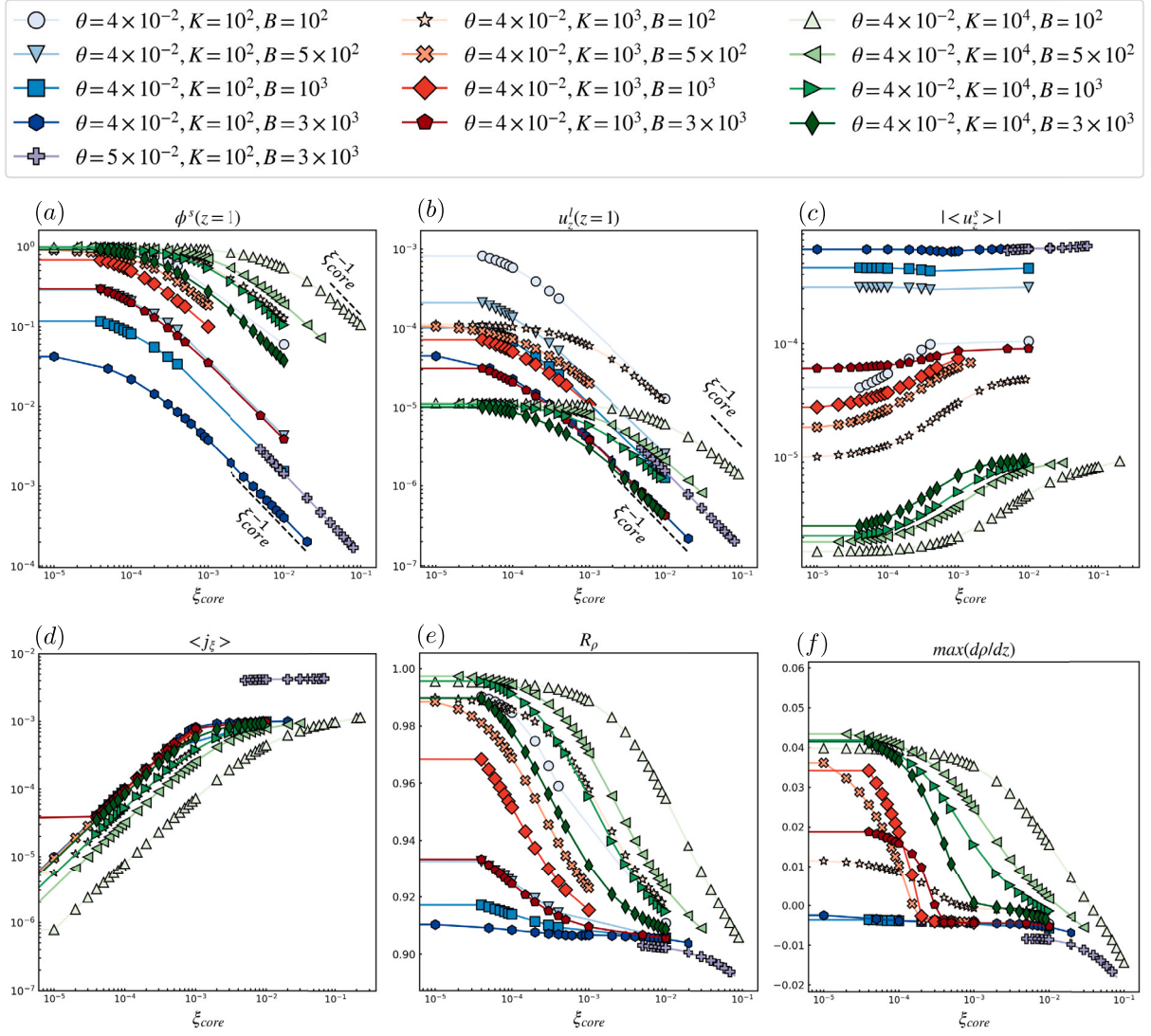


Fig. 2. Variation of (a) the solid volume fraction at top of the layer ($z = 1$), (b) the liquid velocity (at $z = 1$), (c) the average solid velocity, (d) diffusive flux of light element concentration, (e) density contrast between top and bottom of the slurry layer $R_\rho = \bar{\rho}(z = 1)/\bar{\rho}(z = 0)$, (f) maximum gradient of the total density ($d\rho/dz > 0$ - unstable stratification), with respect to ξ_{core} ($\lambda_\eta = 10^4$).

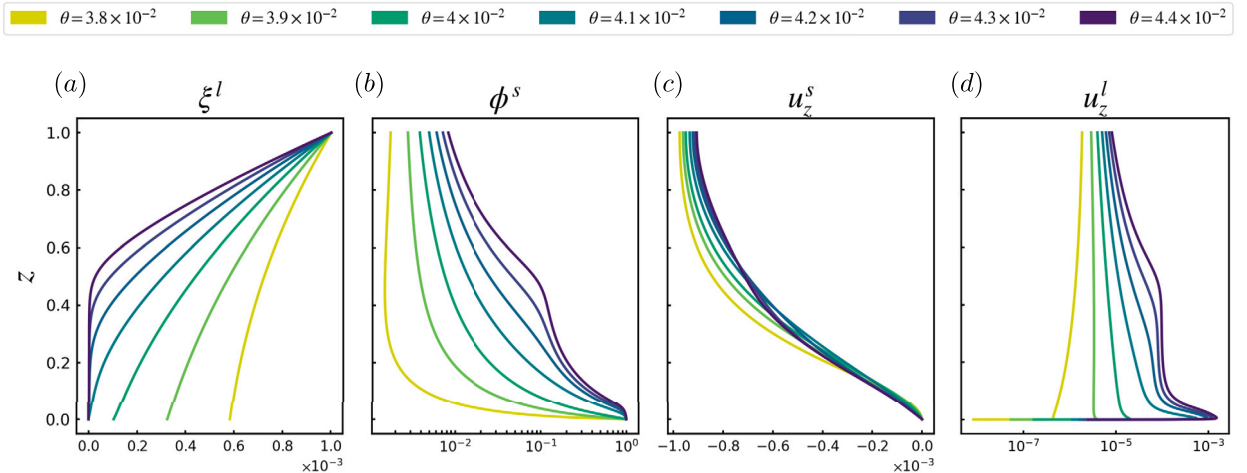


Fig. 3. Profiles of light element concentration ξ^l , solid volume fraction ϕ^s , solid phase velocity u_z^s , liquid phase velocity u_z^l , for increasing values of the ICB heat flux θ ; other parameters are fixed at $B = 3000$, $K = 100$, $\lambda_\eta = 10^4$, $\xi_{core} = 10^{-3}$.

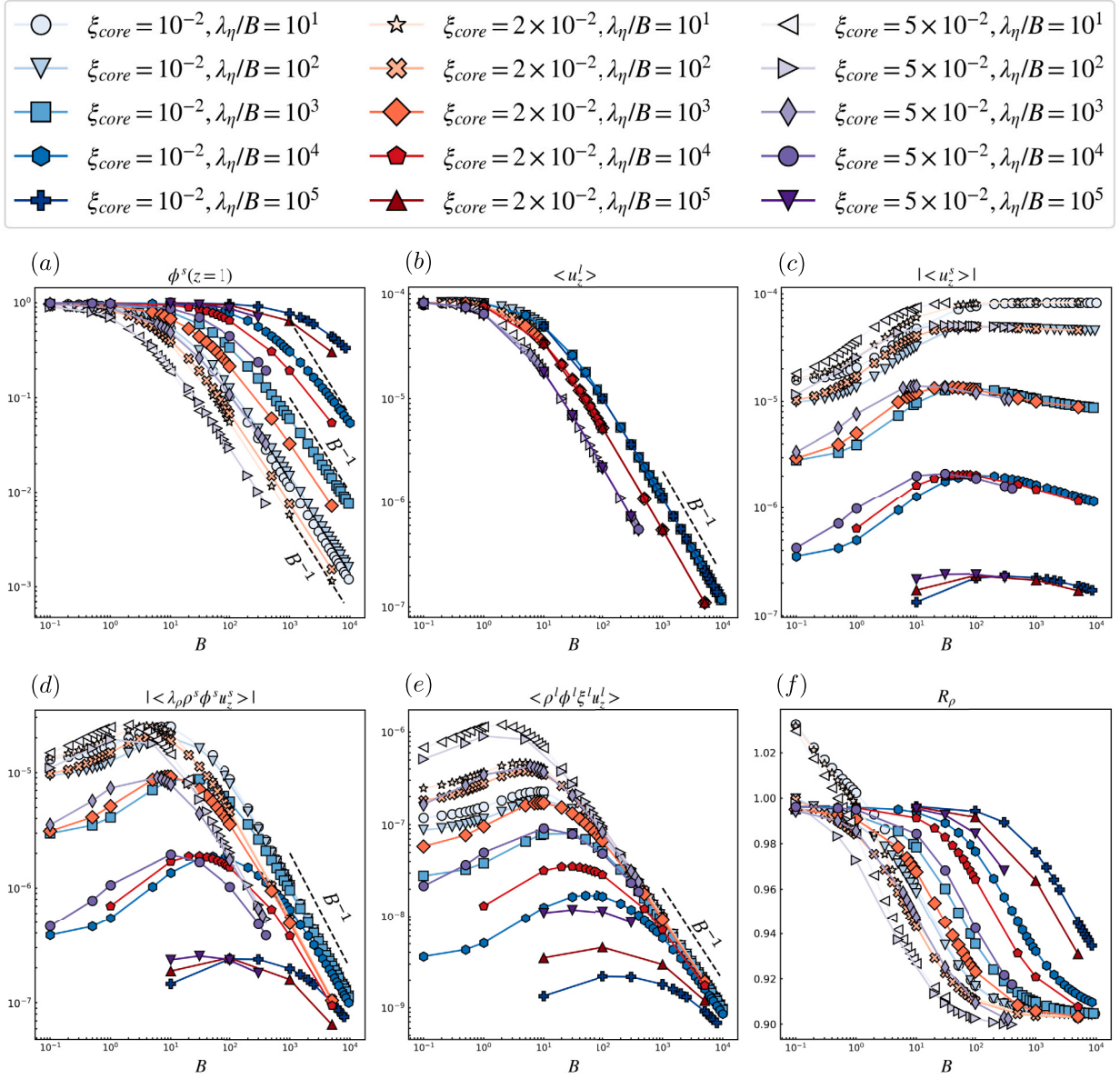


Fig. 4. Variation of (a) solid volume fraction at the top of the slurry layer ($z = 1$); (b) average liquid phase velocity; (c) average solid phase velocity; (d) average solid flux; (e) average light element flux; (f) density ratio between the top and the bottom of the slurry layer, with respect to B at fixed λ_η/B . Other parameters fixed: $K = 1000$, $\theta = 0.04$.

be thought of as quiescent in comparison to the convective outer core (where the average mass flux is much greater).

The density ratio R_ρ for solutions as a function of B and different values of ξ_{core} , and λ_η/B , at fixed $\theta = 0.04$ and $K = 10^3$ is shown in Fig. 4f. In general we have not identified a combination of dimensionless input quantities that delineate the transition from top-heavy (unstable density profile) to bottom-heavy (stable density profile) solutions. However, stable solutions are always obtained as B is increased towards geophysically relevant values, with the density ratio tending to a constant value at modest values of B . We therefore infer that density stratified solutions should be obtained at realistic values of the control parameters.

3.4. Effect of ICB speed, $\mathcal{U} \neq 0$

Up to this point we have considered solutions with $\mathcal{U} = 0$ which allowed us to use simplified boundary conditions (2.11), (2.12). The rationale was that since the movement of the ICB is so slow, $\mathcal{U} \ll 1$, the associated amount of liquid phase consumed and the source of light element are correspondingly negligible. In this section we return to eval-

uate the consequences of this assumption by considering the solutions subject to the true boundary conditions on liquid phase (2.8b) and light element flux (2.8c).

With finite $\mathcal{U} \ll 1$, the physical picture presented in section 2.4 changes slightly. With boundary condition (2.8b), the total mass flux in the layer (2.13) is now

$$\overline{\rho u_z} \equiv \lambda_\rho \phi^s \rho^s u_z^s + \phi^l \rho^l u_z^l = -\lambda_\rho \mathcal{U}. \quad (3.4)$$

Thus, there is downward mass flux on average. Similarly, with boundary condition (2.8c), the light element flux equation (2.14) is now

$$\rho^l \phi^l \left(\xi^l u_z^l - \frac{\tau}{B Pr} \left(\frac{d\xi^l}{dz} + \alpha_\xi^l \chi D \frac{1}{\rho^l} \frac{\xi^l}{T} \frac{dp}{dz} \right) \right) = \rho^l(0) \phi^l(0) \xi^l(0) \mathcal{U}. \quad (3.5)$$

Thus, the total flux (advective and diffusive) of light element concentration is upwards at a constant rate equal to the light element released at the ICB — i.e. $\rho^l(0) \phi^l(0) \xi^l(0) \mathcal{U}$, where $\xi^l(0)$ is the value of ξ^l at $z = 0$ (similarly for ρ^l and ϕ^l).

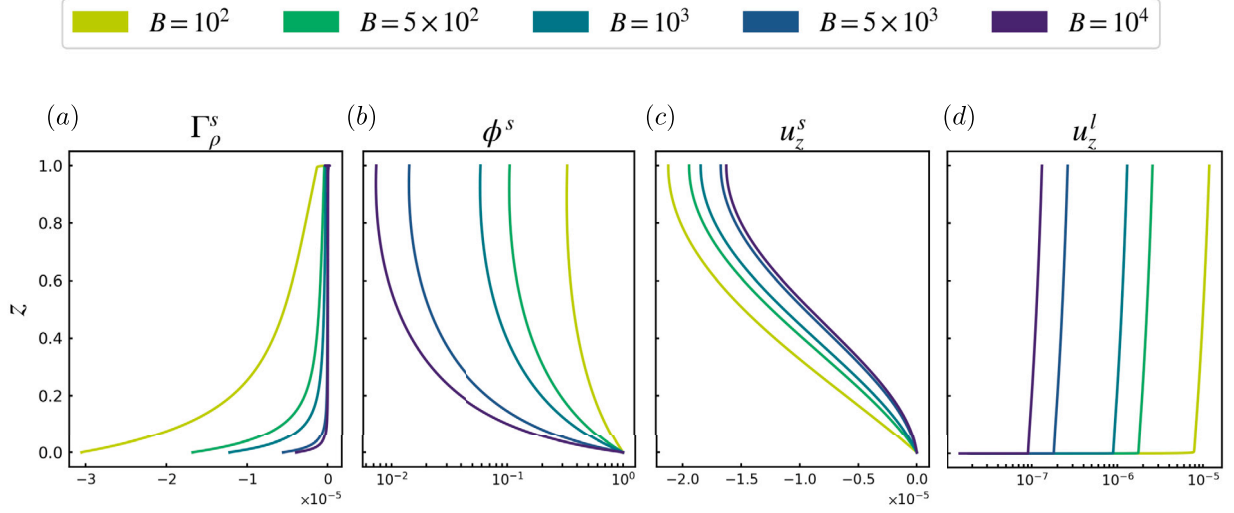


Fig. 5. Profiles of phase change term Γ_{ρ}^s , solid volume fraction ϕ^s , solid phase velocity u_z^s , liquid phase velocity u_z^l for increasing values of the buoyancy number B ; other parameters are fixed at $\lambda_{\eta}/B = 10^3$, $K = 10^3$, $\xi_{core} = 0.01$, $\theta = 0.04$. Note that ϕ^s and u_z^l are plotted on logarithmic axis.

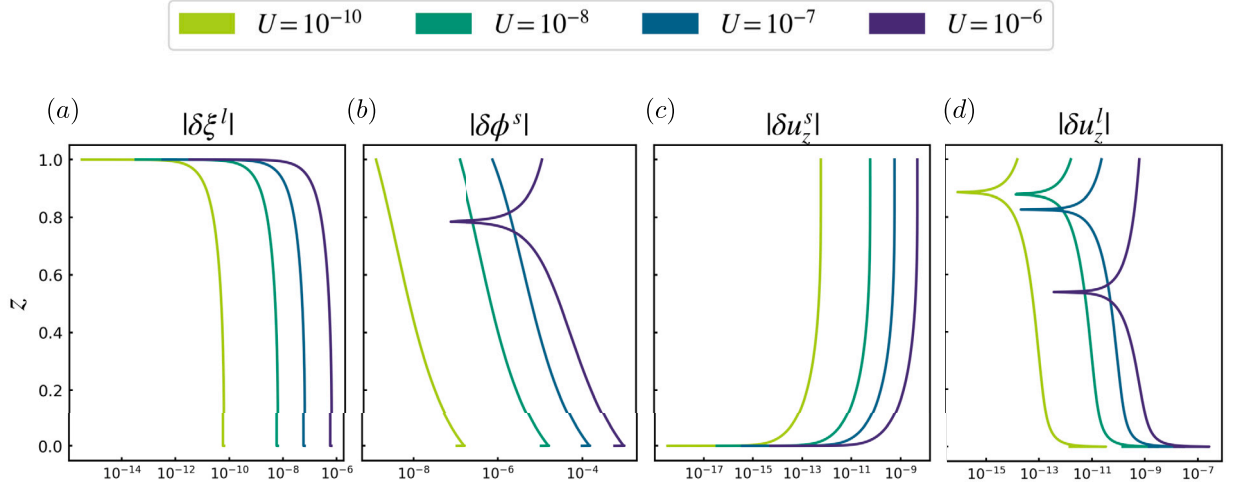


Fig. 6. Absolute difference between solutions with $U \neq 0$ and that with $U = 0$ for increasing values of U . Panels show difference in (a) concentration ξ^l ; (b) solid volume fraction ϕ^s ; (c) solid phase velocity u_z^s ; (d) liquid phase velocity u_z^l . Here, $\theta = 0.04$, $\xi_{core} = 0.01$, $B = 10^3$, $K = 10^3$, $\lambda_{\eta}/B = 10^3$.

We define absolute (δ) and relative (δ^*) differences between any quantity f pertaining to the “true” solution ($U \neq 0$) and the “simplified” solution ($U = 0$), f_0 , as

$$\delta f = f - f_0, \quad \delta^* f = |(f - f_0)/f_0|. \quad (3.6)$$

Fig. 6 shows absolute differences between the solution profiles of the two systems for increasing values of U . The difference between the two sets of solutions is very small, with the biggest contrast being localised predominantly to the thin region directly atop the ICB. Fig. 7 shows the relative differences between the average properties of the solutions with $U \neq 0$ and that with $U = 0$ for increasing values of U . Clearly, the difference between the two sets of solutions is very small, at most 0.01%, and appears to scale with U . Thus, even for values of U much larger than geophysical plausible, non-zero U has negligible effect on the mean properties of solutions.

Caution needs to be taken when extrapolating conclusions to the geophysical scenario, where $B \gg 1$. Recall that as $B \rightarrow \infty$, both solid fraction ϕ^s and liquid velocity u_z^l decrease as B^{-1} , and by extension, so do the solid and liquid mass fluxes. Thus, for sufficiently large B

($B \gg U^{-1}$), solid and liquid fluxes on the left hand side of (3.4) may be comparable in magnitude with the U -term on the right hand side. Clearly, in that case, U may not formally be considered a slight perturbation. Nevertheless, our results with inflated values of U indicate that the difference between the two sets of solutions is localised to the bottom boundary region, with the bulk properties of the solutions being largely unaffected.

In conclusion, the assumption of $U = 0$ in boundary conditions (2.11), (2.12) adequately captures the behaviour of the system, and finite $U \ll 1$ constitutes only a small perturbation on the “simplified” picture.

4. Discussion and conclusions

We have presented the first self-consistent fluid dynamical model of the two-phase two-component slurry F-layer. This formulation generalises the work of Wilczyński et al. (2023) by including a light constituent in the liquid phase and accounting for growth of the solid inner core. The model also improves on the work of Wong et al. (2018, 2021) by directly calculating the solid and liquid velocities, u_z^s and u_z^l , and the

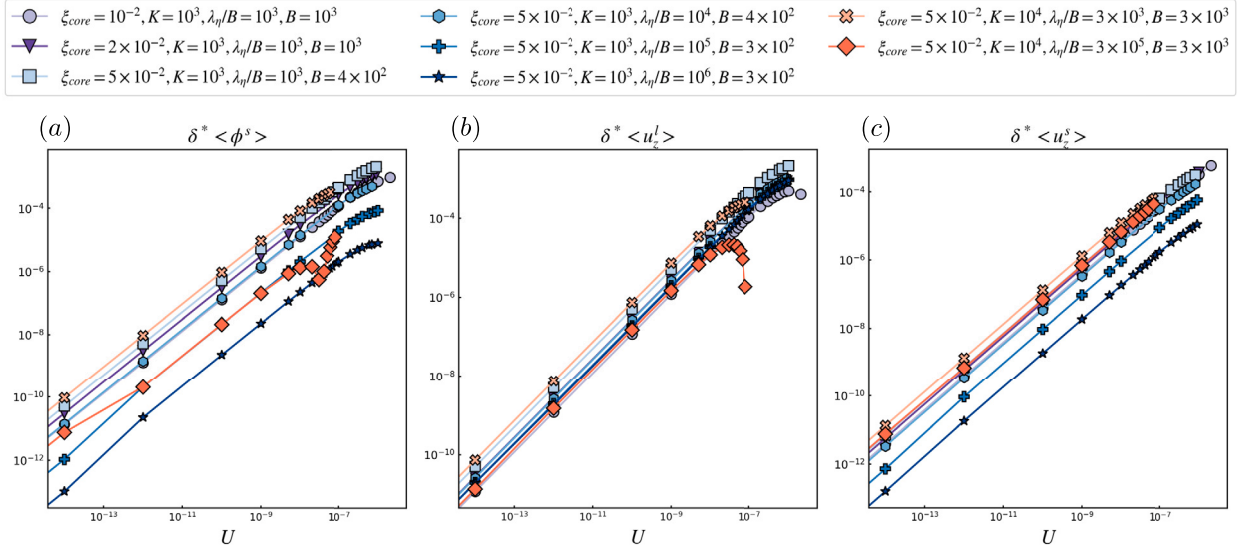


Fig. 7. Relative difference between average properties of the solutions with $U \neq 0$ and that with $U = 0$ for increasing values of U . Panels show difference in (a) the average solid volume fraction, (b) the average liquid velocity, (c) the average solid velocity. Here, $\theta = 0.04$, $K = 10^3$, $\lambda_\eta/B = 10^3$.

solid fraction ϕ^s from momentum and mass conservation respectively. In contrast, Wong et al. (2018, 2021) assumed u_z^l to be negligible and obtained u_z^s and ϕ^s from the solid flux using a mobility model of Stokes flow. This distinction is important because u_z^s , u_z^l , and ϕ^s are not geophysically observable and are hence effectively unknown. Hence it is crucial to have a general model of the slurry F-layer where u_z^s , u_z^l , and ϕ^s are determined self-consistently as a function of the material parameters.

The two-phase two-component slurry model in its most general form is extremely complex and so we have employed several approximations in our numerical solutions (see Wilczyński et al., 2023, for a detailed discussion pertaining to the single component system). The steady, non-rotating and non-magnetic setup enables the governing equations to be solved in 1D, which allows us to explore a wide range of control parameters at conditions far closer to those of the F-layer than would be possible with 2D or 3D solutions. Since the F-layer in most seismic studies is seen as a dominantly 1D structure (Souriau and Poupinet, 1991; Kennett et al., 1995; Zou et al., 2008; Cormier et al., 2011) and is thought to be stably stratified (and therefore not convecting or generating large-scale magnetic field), perturbations to the 1D states we have found may be relatively less important for explaining the available observations. On the other hand, variations in P-wave velocity in the F-layer under Australia and northwestern Pacific suggested by Ohtaki et al. (2018) would require accounting for lateral variations in slurry dynamics. In any case, solving the model system we have derived in 2D or 3D together with the added effects of rotation and magnetism is a daunting computational task that certainly lies outside the scope of this study.

Our solutions assume phase equilibrium and therefore ignore the undercooling that must be present in order to homogeneously nucleate solid phase (e.g. Wilson et al., 2021; Huguet et al., 2023). Classical Nucleation Theory predicts undercooling of 600 – 1000 K to nucleate solids in a range of plausible analogue iron alloys, which is too high to be compatible with the inferred cooling history and present-day thermal structure of the core (Huguet et al., 2018; Davies et al., 2019; Wilson et al., 2023). This so-called “nucleation paradox” demonstrates a fundamental gap in our understanding of how solids form in planetary cores and applies to inner core growth just as it does to the slurry F-layer. Given that the inner core certainly exists, it seems that a resolution to the nucleation paradox will be found and this resolution may help to understand the conditions under which solids can form in the F-layer. On a more practical level, implementing non-equilibrium thermodynamics in the two-phase two-component slurry adds even greater complexity

to the equations and requires macroscopic parameterisations for the microscopic processes of solid nucleation and growth that are poorly understood at present. The assumption of phase equilibrium therefore seems a reasonable one at the present time.

The main result of this work is that stably stratified two-phase two-component slurry solutions can be obtained for a wide range of parameters that span plausible values for Earth’s F-layer. These solutions predict that the solid fraction in the F-layer is very small, $\phi^s \ll 1$, and therefore unlikely to be detected by seismic observations. This implies that sedimentation of solid makes a negligible contribution to inner core growth, which arises almost entirely by direct freezing as in classical models that omit the F-layer (e.g. Labrosse, 2015; Davies, 2015; Nimmo, 2015). We furthermore find that the latent heat transfer within the layer is very small (heat entering the layer at the ICB \sim heat leaving the F-layer), and hence the solutions are consistent with current estimates of the core’s heat budget (e.g. Davies et al., 2015; Nimmo, 2015; Frost et al., 2022). Therefore, notwithstanding the caveats discussed above, we conclude that our slurry model is consistent with theoretical predictions and available observations of the F-layer region.

The basic physical picture of the F-layer suggested by our model essentially refines the picture of Wong et al. (2021) and Gubbins et al. (2008). Thermal conditions are always destabilising in our solutions; the stable stratification is of compositional origin with a reduced light element concentration near the ICB compared to the top of the F-layer. This compositional anomaly is maintained by barodiffusion and outward advection of light material in the liquid. Outward advection is required by mass conservation between falling solid and rising liquid.

Our model predicts the mean velocities of liquid and solid phases, which are not accessible to observation. The liquid velocity is predicted to be very small at core conditions, which is consistent with the assumption of Wong et al. (2021). However, while small, the liquid velocity cannot be neglected as it provides a flux of light material away from the ICB that is crucial for balancing the inward diffusive compositional flux. An estimate for the order of magnitude of solid velocity is given by the ratio of the relative buoyancy between the two phases against the strength of interphase friction, i.e. $\max |u_z^s| \sim (\rho^s - \rho^l)g/(\rho^s c_D)$ (Wilczyński et al., 2023, section 4.3). This gives an estimate for maximum solid velocity on the order of $\sim 5 \times 10^{-5} - 10^{-2} \text{ m s}^{-1}$. Estimated solid velocities in the F-layer are therefore comparable to or smaller than typical core surface flow speeds inferred from geomagnetic secular variation (e.g. Holme et al., 2015; Finlay et al., 2023). Despite such “large” solid phase velocity, the overall solid mass flux $\phi^s \rho^s u_z^s$ is small because the solid

fraction itself is small. Under geophysically relevant conditions where $B \gg 1$, the solid fraction scales as $\phi^s \sim B^{-1}$, and thus solid mass flux also diminishes, $\phi^s \rho^s u_z^s \sim B^{-1}$, when B is increased up to its geophysical value, $B \approx 10^{14}$. Thus, for the F-layer, the overall downward solid flux, and consequent upward flow of liquid phase and light elements, are expected to be very small. Nonetheless, these fluxes are crucial in maintaining stable stratification in the layer whilst also allowing passage of light elements through the layer.

The results of this study suggest that an Earth-like F-layer would be mostly liquid in the bulk, with a narrow “mushy” zone directly above the ICB where solid fractions can be close to unity. The characteristic velocity of the liquid phase in the F-layer is extremely small, and thus the corresponding dynamical time is long compared to the convective overturn time in the liquid outer core. This timescale separation could be exploited in global core dynamo models to study the effect of the expected thermal and compositional anomalies within the F-layer on outer core dynamics and dynamo action without the need to model their two-phase origin.

We believe that the two-phase two-component slurry model developed here is sufficiently general to describe the formation and evolution of the snow layers that have been hypothesised to emerge in a variety of planetary cores including Ganymede (Rückriemen et al., 2015), Mercury (Dumberry and Rivoldini, 2015), and Mars (Davies and Pommier, 2018), as well as Earth’s core. The model predicts a wide range of behaviour, from solid-poor to solid-rich layers, and permits both symmetric and asymmetric phase dynamics depending on the control parameters. Evolving the 1D state in time requires coupling to the evolution of the bulk core, which will add more parameters to an already complex model and would require generalisation of the boundary con-

ditions if the upper and lower boundaries of the slurry both move at different speeds. However, the 1D model could potentially be simplified by exploiting the limiting behaviour of the 1D steady state we have elucidated in this study.

CRedit authorship contribution statement

Fryderyk Wilczyński: Writing – original draft, Investigation, Formal analysis. **Christopher J. Davies:** Writing – original draft, Supervision, Project administration, Funding acquisition, Conceptualization. **Christopher A. Jones:** Writing – review & editing, Supervision, Conceptualization.

Declaration of competing interest

The authors declare that they have no known competing financial interests or personal relationships that could have appeared to influence the work reported in this paper.

Acknowledgements

We are grateful to two reviewers for detailed and constructive comments that helped to improve the manuscript. This work was supported by the Natural Environment Research Council (NERC) grant NE/V010867/1. All solutions presented in this paper were calculated using the open-source Dedalus software (Burns et al., 2020).

Appendix A. Table of parameters

Table A.1
Estimates of physical parameters characterising Inner Core Boundary conditions.

Dimensional parameters				
Symbol	Definition	Estimate	Units	Source
d	depth of the F-layer	1.5×10^5	m	^a
r_i	inner core radius	1.22×10^6	m	^b
g	gravitational acceleration	4.4	m s^{-2}	^b
T_r	reference outer core temperature	5000	K	^c
ρ_r^l	density of liquid iron	12.52×10^3	kg m^{-3}	^d
ρ_r^s	density of solid iron	12.76×10^3	kg m^{-3}	^d
α^l	thermal expansion coefficient (liquid)	$(1.02 - 1.95) \times 10^{-5}$	K^{-1}	^d
α^s	compositional expansion coefficient	1.1		^d
α^s	thermal expansion coefficient (solid)	0.96×10^{-5}	K^{-1}	^e
β^l	isothermal compressibility (liquid)	7.55×10^{-13}	Pa^{-1}	^f
β^s	isothermal compressibility (solid)	7.97×10^{-13}	Pa^{-1}	^g
c_p^l	specific heat capacity (liquid)	715	$\text{J kg}^{-1} \text{K}^{-1}$	^d
c_p^s	specific heat capacity (solid)	750	$\text{J kg}^{-1} \text{K}^{-1}$	^h
k^l	thermal conductivity (liquid)	50 – 107	$\text{W m}^{-1} \text{K}^{-1}$	ⁱ
k^s	thermal conductivity (solid)	286 – 330	$\text{W m}^{-1} \text{K}^{-1}$	^j
η^l	dynamic viscosity (liquid)	10^{-2}	Pa s	^k
η^s	dynamic viscosity (solid)	$10^{11} - 10^{22}$	Pa s	^h
L	latent heat of fusion	0.75×10^6	J kg^{-1}	^d
Q_i	ICB heat flux	$(0.8 - 6) \times 10^{12}$	W	^m
$q = Q_i / (4\pi r_i^2)$	ICB heat flux per unit area	0.04 – 0.32	W m^{-2}	
c_D	inter-phase friction coefficient	8 – 1600	s^{-1}	^o
ξ_{core}	reference oxygen concentration	1 – 5	wt%	ⁿ
\mathcal{R}	universal gas constant	8.3145	$\text{J K}^{-1} \text{mol}^{-1}$	
m_{O}	oxygen molar mass	0.016	kg mol^{-1}	
κ_{O}	oxygen self-diffusion coefficient	10^{-8}	$\text{m}^2 \text{s}^{-1}$	^k
U_{ICB}	ICB velocity	10^{-11}	m s^{-1}	ⁱ

^a Souriau and Poupinet (1991); ^b Dziewonski and Anderson (1981); ^c Nimmo (2015); ^d Gubbins et al. (2004); ^e Vočadlo et al. (1999); ^f Gubbins et al. (2008); ^g Alfè, private communication; ^h Lasbleis and Deguen (2015); ⁱ Davies et al. (2015); ^j Pozzo et al. (2014); ^k Pozzo et al. (2013); ^m Wu et al. (2024); ⁿ Hirose et al. (2013); ^o Wilczyński et al. (2023).

Appendix B. Supplementary material

Supplementary material related to this article can be found online at <https://doi.org/10.1016/j.epsl.2024.119196>.

Data availability

All solutions presented in this paper were calculated using open-source Dedalus software.

References

- Adam, J.-C., Ibouichène, A., Romanowicz, B., 2018. Observation of core sensitive phases: constraints on the velocity and attenuation profile in the vicinity of the inner-core boundary. *Phys. Earth Planet. Inter.* 275, 19–31.
- Alboussiere, T., Deguen, R., Melzani, M., 2010. Melting-induced stratification above the Earth's inner core due to convective translation. *Nature* 466 (7307), 744–747.
- Alfè, D., Gillan, M., Price, G.D., 2002. Composition and temperature of the Earth's core constrained by combining ab initio calculations and seismic data. *Earth Planet. Sci. Lett.* 195 (1–2), 91–98.
- Bercovici, D., Ricard, Y., Schubert, G., 2001. A two-phase model for compaction and damage: 1. General theory. *J. Geophys. Res., Solid Earth* 106 (B5), 8887–8906.
- Burns, K.J., Vasil, G.M., Oishi, J.S., Lecoanet, D., Brown, B.P., 2020. Dedalus: a flexible framework for numerical simulations with spectral methods. *Phys. Rev. Res.* 2 (2), 023068.
- Cormier, V.F., Attanayake, J., He, K., 2011. Inner core freezing and melting: constraints from seismic body waves. *Phys. Earth Planet. Inter.* 188 (3–4), 163–172.
- Davies, C., Pozzo, M., Gubbins, D., Alfè, D., 2015. Constraints from material properties on the dynamics and evolution of Earth's core. *Nat. Geosci.* 8 (9), 678–685.
- Davies, C.J., 2015. Cooling history of Earth's core with high thermal conductivity. *Phys. Earth Planet. Inter.* 247, 65–79.
- Davies, C.J., Mound, J.E., 2019. Mantle-induced temperature anomalies do not reach the inner core boundary. *Geophys. J. Int.* 219 (Supplement_1), S21–S32.
- Davies, C.J., Pommier, A., 2018. Iron snow in the martian core? *Earth Planet. Sci. Lett.* 481, 189–200.
- Davies, C.J., Pozzo, M., Alfè, D., 2019. Assessing the inner core nucleation paradox with atomic-scale simulations. *Earth Planet. Sci. Lett.* 507, 1–9.
- Deguen, R., Alboussiere, T., Brito, D., 2007. On the existence and structure of a mush at the inner core boundary of the Earth. *Phys. Earth Planet. Inter.* 164 (1–2), 36–49.
- Deguen, R., Alboussiere, T., Labrosse, S., 2018. Double-diffusive translation of Earth's inner core. *Geophys. J. Int.* 214 (1), 88–107.
- Drew, D.A., 1983. Mathematical modeling of two-phase flow. *Annu. Rev. Fluid Mech.* 15 (1), 261–291.
- Dumberry, M., Rivoldini, A., 2015. Mercury's inner core size and core-crystallization regime. *Icarus* 248, 254–268.
- Dziewonski, A.M., Anderson, D.L., 1981. Preliminary reference Earth model. *Phys. Earth Planet. Inter.* 25 (4), 297–356.
- Finlay, C.C., Gillet, N., Aubert, J., Livermore, P.W., Jault, D., 2023. Gyres, jets and waves in the Earth's core. *Nature Rev. Earth Environ.* 4 (6), 377–392.
- Frost, D.A., Avery, M.S., Buffett, B.A., Chidester, B.A., Deng, J., Dorfman, S.M., Li, Z., Liu, L., Lv, M., Martin, J.F., 2022. Multidisciplinary constraints on the thermal-chemical boundary between Earth's core and mantle. *Geochem. Geophys. Geosyst.* 23 (3), e2021GC009764.
- Gubbins, D., Alfè, D., Masters, G., Price, G.D., Gillan, M., 2004. Gross thermodynamics of two-component core convection. *Geophys. J. Int.* 157 (3), 1407–1414.
- Gubbins, D., Davies, C., 2013. The stratified layer at the core–mantle boundary caused by barodiffusion of oxygen, sulphur and silicon. *Phys. Earth Planet. Inter.* 215, 21–28.
- Gubbins, D., Masters, G., Nimmo, F., 2008. A thermochemical boundary layer at the base of Earth's outer core and independent estimate of core heat flux. *Geophys. J. Int.* 174 (3), 1007–1018.
- Gubbins, D., Sreenivasan, B., Mound, J., Rost, S., 2011. Melting of the Earth's inner core. *Nature* 473 (7347), 361–363.
- Hirose, K., Labrosse, S., Hernlund, J., 2013. Composition and state of the core. *Annu. Rev. Earth Planet. Sci.* 41, 657–691.
- Holme, R., 2015. Large-scale flow in the core. *Treatise Geophys.* 8, 107–130.
- Huguet, L., Le Bars, M., Deguen, R., 2023. A laboratory model for iron snow in planetary cores. *Geophys. Res. Lett.* 50 (24), e2023GL105697.
- Huguet, L., Van Orman, J.A., Hauck II, S.A., Willard, M.A., 2018. Earth's inner core nucleation paradox. *Earth Planet. Sci. Lett.* 487, 9–20.
- Jephcoat, A., Olson, P., 1987. Is the inner core of the Earth pure iron? *Nature* 325 (6102), 332–335.
- Keller, T., Suckale, J., 2019. A continuum model of multi-phase reactive transport in igneous systems. *Geophys. J. Int.* 219 (1), 185–222.
- Kennett, B.L., Engdahl, E., Buland, R., 1995. Constraints on seismic velocities in the Earth from traveltimes. *Geophys. J. Int.* 122 (1), 108–124.
- Labrosse, S., 2014. Thermal and compositional stratification of the inner core. *C. R. Géosci.* 346 (5–6), 119–129.
- Labrosse, S., 2015. Thermal evolution of the core with a high thermal conductivity. *Phys. Earth Planet. Inter.* 247, 36–55.
- Lasbleis, M., Deguen, R., 2015. Building a regime diagram for the Earth's inner core. *Phys. Earth Planet. Inter.* 247, 80–93.
- Li, Y., Vočadlo, L., Alfè, D., Brodholt, J., 2019. Carbon partitioning between the Earth's inner and outer core. *J. Geophys. Res., Solid Earth* 124 (12), 12812–12824.
- Nimmo, F., 2015. Energetics of the core. *Treatise Geophys.* 8, 27–55.
- Ohtaki, T., Kaneshima, S., 2015. Independent estimate of velocity structure of Earth's lowermost outer core beneath the northeast Pacific from PKiKP - PKPbc differential traveltimes and dispersion in PKPbc. *J. Geophys. Res., Solid Earth* 120 (11), 7572–7586.
- Ohtaki, T., Kaneshima, S., Ichikawa, H., Tsuchiya, T., 2018. Seismological evidence for laterally heterogeneous lowermost outer core of the Earth. *J. Geophys. Res., Solid Earth* 123 (12), 10–903.
- Pozzo, M., Davies, C.J., Gubbins, D., Alfè, D., 2013. Transport properties for liquid silicon-oxygen-iron mixtures at Earth's core conditions. *Phys. Rev. B* 87 (1), 014110.
- Pozzo, M., Davies, C.J., Gubbins, D., Alfè, D., 2014. Thermal and electrical conductivity of solid iron and iron–silicon mixtures at Earth's core conditions. *Earth Planet. Sci. Lett.* 393, 159–164.
- Roberts, P.H., Loper, D.E., 1987. Dynamical processes in slurries. In: *Structure and Dynamics of Partially Solidified Systems*. Springer, pp. 229–290.
- Rückriemen, T., Breuer, D., Spohn, T., 2015. The Fe snow regime in Ganymede's core: a deep-seated dynamo below a stable snow zone. *J. Geophys. Res., Planets* 120 (6), 1095–1118.
- Souriau, A., Poupinet, G., 1991. The velocity profile at the base of the liquid core from PKP (BC + Cdiff) data: an argument in favour of radial inhomogeneity. *Geophys. Res. Lett.* 18 (11), 2023–2026.
- Stevenson, D., 1987. Limits on lateral density and velocity variations in the Earth's outer core. *Geophys. J. Int.* 88 (1), 311–319.
- Vočadlo, L., Brodholt, J., Alfè, D., Price, G.D., Gillan, M.J., 1999. The structure of iron under the conditions of the Earth's inner core. *Geophys. Res. Lett.* 26 (9), 1231–1234.
- Wilczyński, F., Davies, C.J., Jones, C.A., 2023. A two-phase pure slurry model for planetary cores: one-dimensional solutions and implications for Earth's F-layer. *J. Fluid Mech.* 976, A5.
- Wilson, A.J., Alfè, D., Walker, A.M., Davies, C.J., 2023. Can homogeneous nucleation resolve the inner core nucleation paradox? *Earth Planet. Sci. Lett.* 614, 118176.
- Wilson, A.J., Walker, A.M., Alfè, D., Davies, C.J., 2021. Probing the nucleation of iron in Earth's core using molecular dynamics simulations of supercooled liquids. *Phys. Rev. B* 103 (21), 214113.
- Wong, J., Davies, C.J., Jones, C.A., 2018. A Boussinesq slurry model of the F-layer at the base of Earth's outer core. *Geophys. J. Int.* 214 (3), 2236–2249.
- Wong, J., Davies, C.J., Jones, C.A., 2021. A regime diagram for the slurry F-layer at the base of Earth's outer core. *Earth Planet. Sci. Lett.* 560, 116791.
- Wu, R., Xiang, S., Sun, Y., Xian, Y., Luo, Y., Dai, F., 2024. Obtaining the equation of state for multiphase iron under Earth's core conditions using Bayesian statistics. *ESS Open Arch.*
- Zhang, Y., Nelson, P., Dygert, N., Lin, J.-F., 2019. Fe alloy slurry and a compacting cumulate pile across Earth's inner-core boundary. *J. Geophys. Res., Solid Earth* 124 (11), 10954–10967.
- Zou, Z., Koper, K.D., Cormier, V.F., 2008. The structure of the base of the outer core inferred from seismic waves diffracted around the inner core. *J. Geophys. Res., Solid Earth* 113 (B5).